Xiaodong Ji*, Xiang Gao, Yuncheng Zhuang, Zhe Qu. Enhanced measurements of structural inter-story drift responses in shaking table tests. Engineering Structures, 2023, 278: 115508.

Please cite this article as: Xiaodong Ji*, Xiang Gao, Yuncheng Zhuang, Zhe Qu. Enhanced measurements of structural inter-story drift responses in shaking table tests. Engineering Structures, 2023, 278: 115508.

Enhanced measurements of structural inter-story drift responses in shaking table tests

Xiaodong Ji[a*], Xiang Gao[a], Yuncheng Zhuang[a], Zhe Qu[b]

[a] *Key Laboratory of Civil Engineering Safety and Durability of China Education Ministry, Department of Civil Engineering, Tsinghua University, Beijing 100084, China,*

[b] *Key Laboratory of Earthquake Engineering and Engineering Vibration, Institute of Engineering Mechanics, China Earthquake Administration, Harbin, China*

Abstract: Accurate measurements of inter-story drift responses are critical in shaking table tests. This paper compared three commonly-used approaches of inter-story drift measurement, and developed the techniques for enhanced measurement. This study proposed a novel arrangement of displacement meters along with the associated data correction method. By setting the overhanging steel arms above and beneath a floor slab at the same position, the suggested approach could remove the influence of floor slab rotation and thus improve the accuracy of inter-story drift measurement. In addition, a novel computer vision-based target tracking approach based on a super-resolution (SR) image reconstruction technique was developed. This advanced deep learning-based SR method can transform blurry, low-resolution images into sharp, high-resolution ones for precise target tracking. The accuracy of these developed inter-story measurement approaches was evaluated through a case study of shaking table tests of a large-scale three-story reinforced concrete (RC) building structure. The results indicated that the novel arrangement of displacement meters and associated data correction method successfully eliminated the influence of floor slab rotation, which could result in an error of approximately 20% in the inter-story drift measurement if left uncorrected. The novel SR method overcame the limitation of video resolution and achieved a stable sub-

* **Correspondence:** Xiaodong Ji, Department of Civil Engineering, Tsinghua University, Beijing 100084, China.
Email: jixd@mail.tsinghua.edu.cn

pixel measurement result. In the case of seismic loading, the SR method improved the signal-to-noise ratio of the drift measurement by 68%, and reduced the root mean square error by 63%, compared with the conventional template matching technique. The modal parameters of the test structure were accurately identified from the small-magnitude displacement data of white noise vibration responses measured using the SR method.

Keywords: inter-story drift measurement; shaking table test; super-resolution reconstruction; computer vision; displacement meter arrangement

1 INTRODUCTION

Shaking table tests are widely used to simulate the dynamic responses of building structures subjected to seismic motions [1-4]. One of the main measurements in shaking table tests is inter-story drift, which is an important indicator of structural seismic performance [5]. Currently, inter-story drifts are usually measured by displacement meters, acceleration integration, and computer vision-based methods.

A displacement meter is a conventional instrument for displacement measurement that can directly measure the relative displacement between two points. As depicted in Fig. 1, there are two types of common arrangements of displacement meters for measuring inter-story drifts in shaking table tests. In the first type, the displacement meters are positioned outside the shaking table and connected to a fixed platform. This arrangement requires displacement meters with a large measurement range as the movement of the shaking table is also included in the measurement. In this case, the accuracy of measuring a small magnitude response is inevitably sacrificed because of limited the resolution of large-range displacement meters. In the second type, the displacement meters are arranged inside the test structure. Yu et al. [6] utilized displacement meters to measure the change in the diagonal distance between two columns, and to calculate inter-story drifts (Fig. 1). The diagonal displacement meter included a linear variable differential transformer (LVDT) connected to a spring wire which extended the measurement distance. However, the accuracy of the measurement was affected by the sagging of the wire. Kajiwara et al. [7] set overhanging steel arms between adjacent floors in a full-scale shaking table test structure and mounted the displacement meters within those overhanging arms (Fig. 1). While this arrangement provided a direct measurement of inter-story drifts, it can be influenced by floor slab rotation which induces the rotation of the overhanging arms. To accurately and conveniently measure the structural displacement, further research is needed to determine how to arrange the displacement meters reasonably.

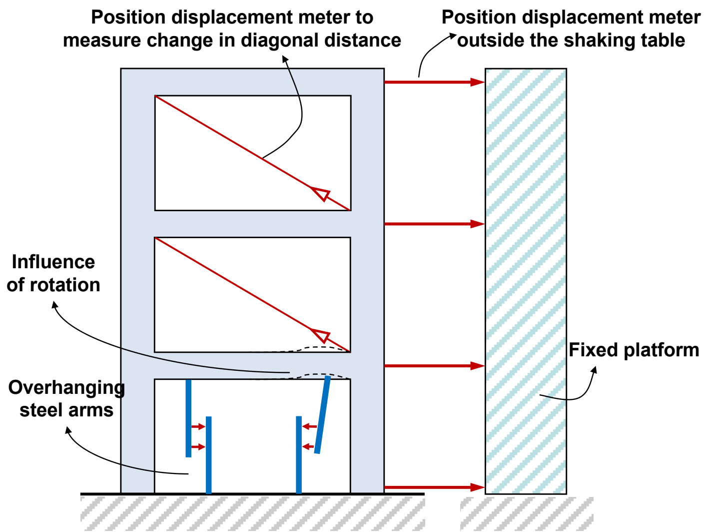

Fig. 1. Arrangement of displacement meters

In general, accelerometers are used in shaking table tests to measure the floor acceleration responses of the test structure [8-10]. While the structural displacement can be calculated by double integrating the recorded acceleration, non-negligible low-frequency noises in acceleration measurement may lead to significant baseline drift when integrating acceleration data [11-13]. Nevertheless, the acceleration integration approach is used for displacement measurement in some shaking table tests and seismic structural health monitoring systems [14, 15], if the installation of displacement meters is difficult and costly. Baseline correction is necessary for the acceleration integration, and the commonly used methods for baseline correction include piecewise corrections to displacement, elimination of polynomial trends in velocity and displacement, and high-pass filtering [16-18]. As the baseline correction (e.g., filtering the low-frequency response data) in acceleration integration may lead to nonnegligible error in the displacement estimation particularly when the structure undergoes nonlinear responses, it is a clear need to quantify and discuss the error range of this approach.

Computer vision-based measurement methods track the displacement of targets or feature points in a video to calculate the actual displacement of a structure. According to different tracking algorithms, computer vision-based measurement methods can be categorized into cross-correlation template matching [19], geometric matching [20], color matching [21], optical flow tracking [22, 23], feature point tracking [24], deep learning-based tracking [25], and others. The accuracy of vision-based measurement depends on image resolution, which is related to the camera parameters and shooting distance. In large-scale shaking table tests, a long shooting distance is often necessary to ensure a full-field view of the movement of a large structure specimen, resulting in low-resolution (LR) video images. It is a challenge to accurately capture small displacements from these LR images. The recently developed super-resolution (SR) techniques provided potential to enhance the accuracy of vision-based measurement using consumer-grade cameras [26-32].

The objective of this paper is to compare the commonly-used approaches of inter-story drift measurement in shaking table tests and to develop the associated techniques for improvement of the measurement accuracy. The major contributions of this paper are threefold. Firstly, a novel arrangement of displacement meters and the associated data correction method were proposed for shaking table tests. The method can accurately measure the inter-story drifts by eliminating the influence of floor slab rotations. Secondly, a novel object tracking method based on SR image reconstruction was proposed to overcome the resolution limitation of images. The SR target tracking method realized stable sub-pixel displacement measurement by a combination of deep learning-based SR techniques and conventional cross-correlation template matching algorithms. Thirdly, shaking table tests of a large-scale three-story reinforced concrete (RC) building structure were used as a case study to validate these developed methods. The accuracy of various measurement methods was compared using the test data.

This paper is organized as follows. Section 2 presents the novel arrangement of displacement meters, the associated data correction method, and the novel SR target tracking method. Section 3 describes the experimental program and instrumentation of the shaking table tests on a three-story RC structure. Section 4 presents a detailed comparison of the inter-story drift measurement results of experimental tests using three different approaches. Section 5 discusses a few issues that arose in relation to the developed inter-story measurement approaches.

2 DEVELOPMENT OF INTER-STORY DRIFT MEASUREMENT APPROACHES

2.1 Arrangement and data correction for displacement meter measurement

Fig. 2(a) depicts a common arrangement of the displacement meters in shaking table tests [7]. An improved arrangement is proposed to eliminate the influence of floor slab rotation, as presented in Fig. 2(b). In this arrangement, the overhanging steel arms above and beneath a floor slab are placed in the same position, which ensures the rotation angles of the two steel arms are identical. This makes it possible to calculate the relative rotation angle α between the upper steel arm and the lower steel arm (Fig. 3), and thus, the original measured inter-story drift data can be corrected to remove the influence of floor slab rotations. It should be noted that the novel approach needs two displacement meters installed on a pair of steel arms, while one displacement meter would be fine for the conventional approach. This is the additional cost of the novel approach for enhancing the measurement accuracy.

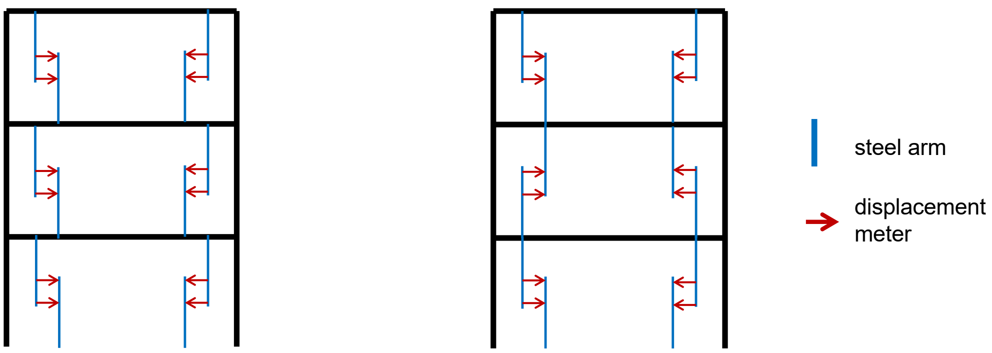

(a) Arrangement in Reference [7] (b) Improved arrangement

Fig. 2. Arrangement of steel arms and displacement meters

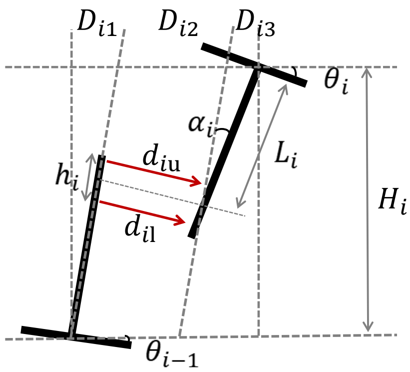

Fig. 3. Displacement measurement correction

The actual inter-story drift can be calculated from the displacement meter measurement results using the following equations:

$$D_{if} = D_{i1} + D_{i2} + D_{i3} \tag{1}$$

$$D_{i1} = \theta_{i-1} H_i = \sum_{k=0}^{i-1} \alpha_k H_i \tag{2}$$

$$D_{i2} = (d_{iu} + d_{il})/2\cos\theta_{i-1} \tag{3}$$

$$D_{i3} = \alpha_i L_i \tag{4}$$

$$\alpha_i = arctan[(d_{iu} - d_{il})/h_i] \tag{5}$$

In Eqs. (1) - (5), D_{if} is the actual inter-story drift, namely, the corrected inter-story drift measurement; D_{i1} is the drift caused by the rotation of the lower steel arm; D_{i2} is the mean measured value of displacement meters, that is the original inter-story drift measurement; D_{i3} is the displacement caused by the relative rotation between the upper and lower steel arms; θ_i is the local rotation angle of the i-th floor relative to the shaking table; H_i is the height of the i-th story; α_i is the relative rotation angle between the upper steel arm and the lower steel arm, in particular $\alpha_0 = 0$; d_{iu} is the measured value of the upper displacement meter; d_{il} is the measured value of the lower displacement meter; L_i is the distance from the upper floor slab to the centroid of two displacement meters; and h_i is the distance between two displacement meters. When $(d_{iu} - d_{il})/h_i < 0.4$, Eq. (5) can be simplified as Eq. (6) with an error no more than 5%.

$$\alpha_i = (d_{iu} - d_{il})/h_i \quad (6)$$

2.2 SR target tracking method

Cross-correlation template matching is a widely employed target tracking method [33-35], which can track the artificial target, apparent texture, or rigid regions of a structure. The SR technique is used to enhance tracking accuracy, which can convert blurry, LR images into sharp, SR ones, providing more refined image data by increasing the number of pixels per unit area. Depending on the reconstruction mechanism, the SR technique can be classified into four categories: interpolation [36, 37], degradation [38], machine learning [39] and deep learning [40] models. Among these, the SR technique based on deep learning is conspicuous for its superior reconstruction performance because of the powerful learning capability of neural networks [41].

In this study, an advanced lightweight SR recurrent neural network (RNN) [42]was trained. The architecture of the lightweight SR network was developed by Li et al. [42]. As depicted in Fig. 4, the network can be unfolded to T iterations, and the loss functions of each iteration are identical (Eq. (7)). In each iteration, two convolutional layers are used to extract shallow features of the input LR image. A feedback block (FB) is designed to receive the shallow features and handle the iteration information flows, and the remaining deconvolutional and convolutional layers are utilized to receive the output of the FB and generate a residual image I_{Res}. The output SR image is obtained by adding the residual and the upsampled images. Because of the recurrent network architecture, the SR model can deliver great reconstruction performance by using much fewer parameters compared with other state-of-the-art models.

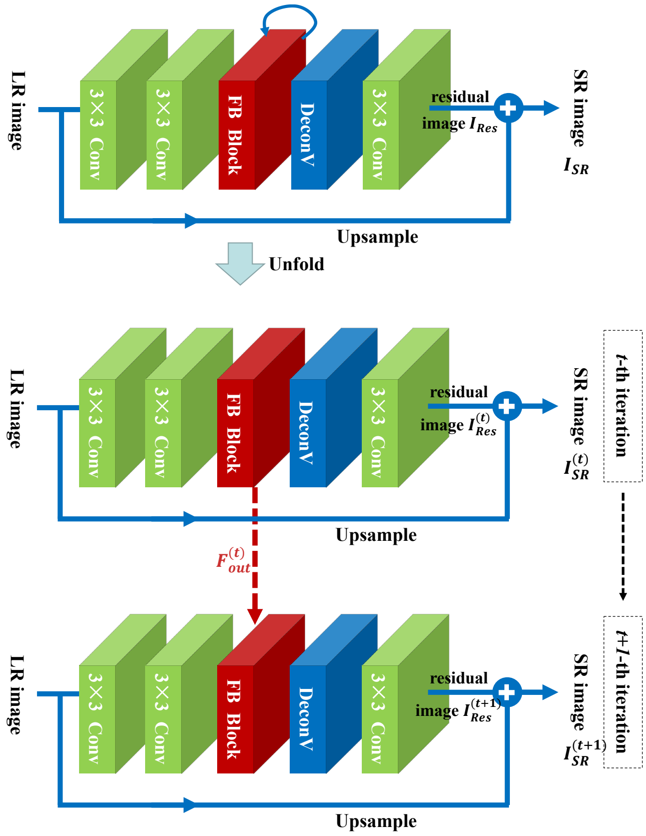

Fig. 4. The architecture of the SR neural network

$$L(\theta) = 1/T \sum_{t=1}^{T} W^{(t)} \left\| I_{HR}^{(t)} - I_{SR}^{(t)} \right\|_1 \tag{7}$$

In Eq. (7), θ is the parameters of the network, t is the iteration index, $W^{(t)}$ is the weight factor of the output at the t-th iteration (defined as $W^{(t)}$=1 in this study), $I_{HR}^{(t)}$ is the target high-resolution (HR) image, and $I_{SR}^{(t)}$ is the output SR image at the t-th iteration, $\|*\|_1$ is the L1 norm regularization.

This study optimized the network only for regions of interest (ROIs) to minimize computation cost. ROIs are the regions containing the artificial targets which need to be tracked. Images with geometric features similar to the artificial targets in the test were created with MATLAB, and pasted on different backgrounds. The dataset for the SR neural network consisted of both HR images and the corresponding LR images. The pasted images were photographed with a set size of 400×400 pixels as the HR images. The LR images were created by downsampling the HR images to a size of 50×50 pixels. The 1/8 size ratio of HR images to LR images allowed the trained network to transform the input blurry image into an SR image which was 8 times the size larger. The LR dataset was then randomly divided into three groups, one of which group applied Gaussian noise, whereas another applied Gaussian blur, to ensure the generalizability of the network. A total of 104 HR images were taken under different backgrounds, lighting conditions, shooting angles and distances, to ensure the trained model can adapt to different situations. Among these, 83 images were randomly selected for the training dataset, and the other images were left for validation. The diversity of the datasets was enriched by random rotation and flipping, adjustment of brightness, and saturation. After the data augmentation, the training and validation datasets consisted of 996 and 252 images, respectively.

The image quality of SR reconstruction was assessed using three indicators: the peak signal-to-noise ratio (PSNR), structural similarity index measure (SSIM) [43], and Pearson correlation coefficient. The PSNR and SSIM values can be calculated by Eqs. (8) - (10). For the purpose of comparison, the images were also handled using a commonly used bicubic interpolation (BI) reconstruction. Table 1 summarizes the values of assessment indicators for the reconstructed images of the testing dataset. Four sets of example images with different sizes, backgrounds, lighting conditions, shooting angles, and distances are presented in Fig. 5. These indicate that SR reconstruction achieves a superior performance than BI reconstruction in different situations.

$$PSNR = 10 \cdot log_{10}(MAX^2/MSE) \tag{8}$$

$$SSIM = \frac{(2\mu_X\mu_Y + C_1)(2\sigma_{XY} + C_2)}{(\mu_X^2 + \mu_Y^2 + C_1)(\sigma_X^2 + \sigma_Y^2 + C_2)} \tag{9}$$

$$\sigma_{XY} = \frac{1}{N-1}\sum_{i=1}^{N}(X_i - \mu_X)(Y_i - \mu_Y) \tag{10}$$

In Eqs. (8) - (10), MAX is the maximum pixel value of the image (defines as $MAX = 255$ in this study), MSE is the mean square error of image X and image Y; X_i and Y_i are the luminance intensity of each pixel in image X and image Y; μ_X and μ_Y are the mean luminance intensity of image X and image Y; σ_X and σ_Y are the standard deviation of the luminance of image X and image Y; C_1 and C_2 are constants (defines as $C_1 = C_2 = (0.01 \times 255)^2$ in this study); and σ_{XY} is the covariance of image X and image Y.

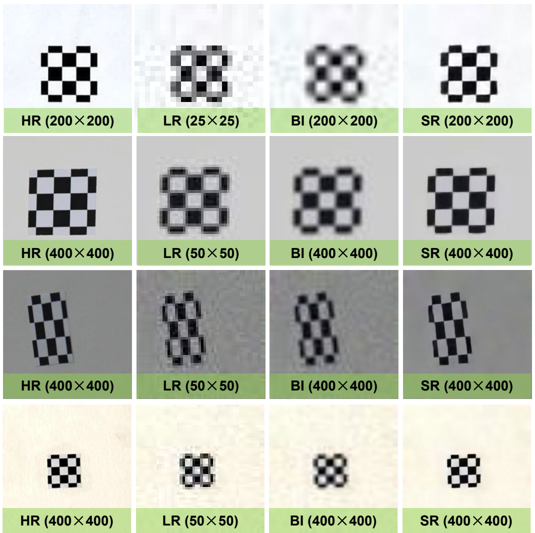

Fig. 5. Visual comparison of BI and SR

Table 1 Quantitative evaluation of BI and SR

	PSNR（dB）	SSIM	Correlation coefficient
SR	29.40	0.933	0.986
BI	17.76	0.618	0.909

A position tracking procedure for each ROI, which combined the traditional template matching approach with the SR technique, was developed as shown in Fig. 6(a). The procedure consists of the following steps: (1) Select a region with fixed apparent features, i.e. the region containing an artificial target, as the ROI, and use the template matching method to track its position (x_a, y_a); (2) Crop and save the ROI; (3) Reconstruct the ROI using the SR technique; (4) Select several objects of interest (OOIs) within the ROI and capture their position using the template matching method to determine the relative coordinates of the target centroid (x'_b, y'_b); (5) Calculate the accurate coordinates of the target centroid (x_b, y_b) by adding the relative coordinates of target centroid and the coordinates of the ROI. It is noted that the pre-trained SR model can be used for different sizes of ROI, as shown in Fig. 5. As a large size of ROI results in an increased computation cost, it is recommended to select an ROI of which the size is slightly larger than the target.

In this study, the corners of the target were chosen as OOIs, as shown in Fig. 6(b). The accurate coordinate of the target centroid was calculated by adding the coordinate of the ROI in the global image (x_a, y_a) and the relative coordinate of the target centroid in the ROI (x'_b, y'_b). The relative coordinate of target centroid was determined by the geometric operation of the coordinates of OOIs. If the errors of the OOI tracking results are independent and identically distributed, the use of an increased number of OOIs can lead to improved accuracy with less error variance. Further discussion on multi-region tracking can be found in Section 5.2.

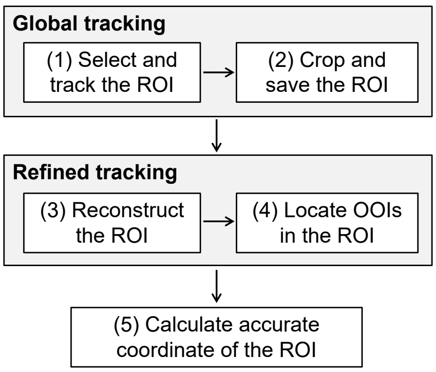

(a) Position tracking procedure for ROI

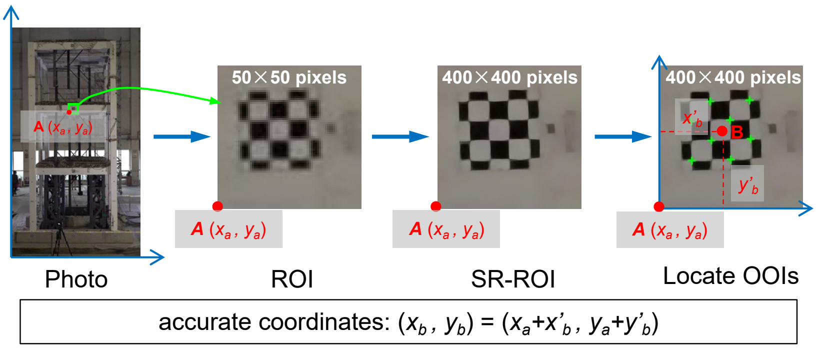

(b) Coordinate calculation

Fig. 6. Flowchart of the SR target tracking method

3 THREE-STORY RC STRUCTURE EXPERIMENT

3.1 Experimental program

The specimen was a 1/2-scale three-story RC building structure. As shown in Fig. 7, it had a plan dimension of 4.7 m (wall direction) by 3.0 m (frame direction) and a uniform story height of 2.3 m. Details of the specimen design can be found in Ji et al. [44]. Two seismic motions, the JMA Kobe and Takatori recorded in the 1995 Kobe earthquake, were selected for the shaking table input motions. The seismic motions were scaled to four levels: peak ground acceleration = 0.07, 0.20, 0.40 and 0.62 g. During the tests, a total of six seismic shakings were applied in both the wall and frame directions: JMA Kobe 0.07g (Case 1), JMA Kobe 0.20g (Case 2), JMA Kobe 0.40g (Case 3), JMA Kobe 0.62g (Case 4), Takatori 0.40g (Case 5), Takatori 0.62g (Case 6). For each case, the seismic motion was firstly applied in the wall direction and then in the frame direction. Before and after each seismic motion shaking event, the bidirectional white noise was input to the shaking table to induce low-magnitude vibrations of the specimen that were used for system identification. The white noise had a bandpass frequency of 0.5-50 Hz, a root mean square magnitude of 15 gal and a duration of 240 s.

Three inter-story drift measurement approaches were implemented in the shaking table tests: displacement meter measurement, acceleration integration measurement and computer vision-based measurement. A total of 16 accelerometers were installed to measure the accelerations of each floor and shaking table, and 18 displacement meters were used to measure the inter-story drifts. Fig. 8 depicts the arrangement of accelerometers and displacement meters in a typical floor. Video cameras were arranged outside the table to record the vibrations of the specimen.

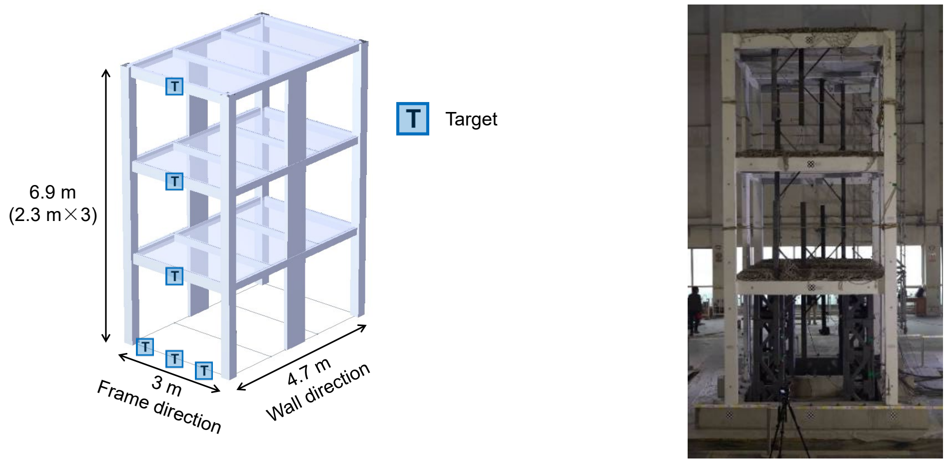

（a） Schematic drawing　　　　（b） Photograph

Fig. 7. Overview of the specimen

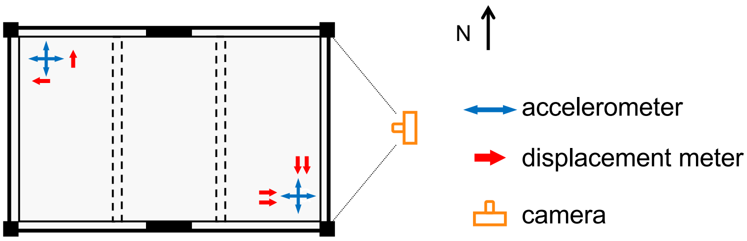

Fig. 8. Arrangement of instrumentation

3.2 Displacement meter measurement

Two sets of overhanging steel arms were arranged on each floor, among which one group of steel arms and two displacement meters were arranged as depicted in Fig. 2(b). The displacement meters used in the tests were laser displacement meters and string potentiometers. The laser displacement meters offered a repeat accuracy of 0.2 mm and a measurement range of 80 mm. The string potentiometers had a repeat accuracy of 0.15 mm and a measurement range of 75 mm. The steel arms were rigid and securely fixed to the floor slabs by anchor bolts, with a calculated natural vibration frequency of 312 Hz. This prevented their vibrations from influencing the displacement meter measurement. The displacement measurement was recorded at a sampling frequency of 200 Hz.

3.3 Acceleration integration measurement

The accelerometers had a measurement range of ± 5 g and frequency bandwidth of 0-2500 Hz. Accelerations were recorded at a sampling frequency of 256 Hz. The following procedure was employed to calculate the inter-story drifts from the measured acceleration data.

(1) Remove the pre-event mean accelerometer measurement data.

(2) Use a low-pass filter to remove high-frequency noise from the acceleration data. The cut-off frequency of this test was designated as 25 Hz considering the structural natural frequency.

(3) Apply high-pass filtering to the acceleration data to eliminate possible baseline drift, and integrate the filtered acceleration to obtain the velocity. Next, use high-pass filtering on the velocity to eliminate the trend error caused by numerical integration [45] and integrate the filtered velocity to obtain the displacement. A 4-pole acausal Butterworth filter was utilized in the analysis. As the key parameter, the cutoff frequency was determined from the peak point of the signal-to-noise ratio (SNR) curve [12], as depicted in Fig. 9. The SNR was calculated as follows:

$$SNR = 10 \cdot \log_{10}(R/N) \quad (11)$$

where R is the power of the real signal and N is the power of the noise. In this equation, the displacement meter measurement results were used as the real signal, and the noise was defined as the error between the acceleration integration results and the displacement meter measurement. The acceleration integration results were resampled to 200 Hz (i.e., the sampling frequency of displacement meters) in the noise calculation.

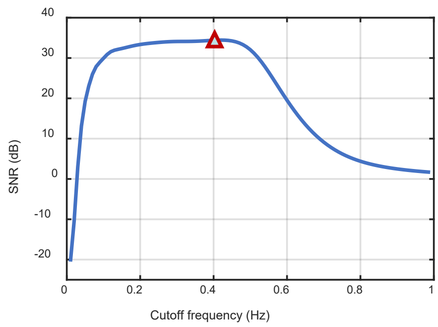

Fig. 9. Optimal cutoff frequency

3.4 Computer vision-based measurement

Experimental videos were taken using a Nikon D750 camera with an AF-S NIKKOR 24-120 mm lens. This is a consumer-grade digital camera equipped with a standard zoom lens and a CMOS (complementary metal oxide semiconductor) image sensor with a size of 35.9 ×24 mm. The optical axis of the camera was configured to be as perpendicular to the front surface of the specimen as possible. The shooting distance (i.e., the distance between the camera and the test specimen) was not measured. The experimental videos had a frame rate of 50 Hz with an image resolution of 1920 × 1080 pixels. Artificial targets were affixed to the surface of the frame beams and foundation beam of the specimen.

Lens distortion correction is a necessary step when processing photos that are shot using a wide-angle lens. As the videos were taken using an ordinary lens, and only the in-plane motion of the structure was considered, the method of calculating the scale factor at each floor was adopted to simplify the distortion correction process [46]. The scale factor, which converts pixels to engineering units such as millimeters, was calculated according to Eq. (12), utilizing the beams of each floor as the object. The scale factors at different heights in the photos were calculated, yielding values of approximately 4.5 mm/pixel. This means that the minimum resolution of the template matching method was 4.5 mm. As the SR method in this study can transform one LR image into an SR image with the size enlarged by 8 times, it resulted in an improved minimum resolution of 4.5 / 8 = 0.56 mm. It should be noted that the scale factor varies for different sizes of the observed object and camera resolutions. After obtaining the coordinate changes of the target in the videos, the actual displacement was calculated as follows:

$$\alpha = \frac{D}{d} \tag{12}$$

$$\Delta x = \lambda \alpha \tag{13}$$

In Eqs. (12) and (13), α is the scale factor; D is the engineering length of the selected object; d is the image pixels of the selected object; Δx is the actual displacement of the ROI; and λ is the coordinate changes of the ROI in the video.

4 EXPERIMENTAL RESULTS

In this section, the effect of the displacement meter data correction method was evaluated, and the influence of floor slab rotation on structural displacement measurement was quantified and eliminated. The results of acceleration integration measurement and computer vision-based techniques were evaluated for the six seismic loading cases (Case 1 - 6) and four white noise excitation cases in the frame direction. To evaluate the measurement accuracy, two indicators were applied: SNR and root mean square error (RMSE) which reflect the relative error rate and the absolute error, respectively.

4.1 Displacement meter measurement results

Fig. 10 presents the power spectrum of the measured data of the second story inter-story drift response for seismic Case 3. As indicated, the corrected data had an increased level of high-frequency noise because the calculation in Eqs. (1) - (6) amplified the noise. A detailed discussion of noise amplification can be found in Section 5.1. To suppress the adverse influence of the high-frequency noise, the measured inter-story drift data was filtered using a low-pass filter with a cutoff frequency of 5 Hz.

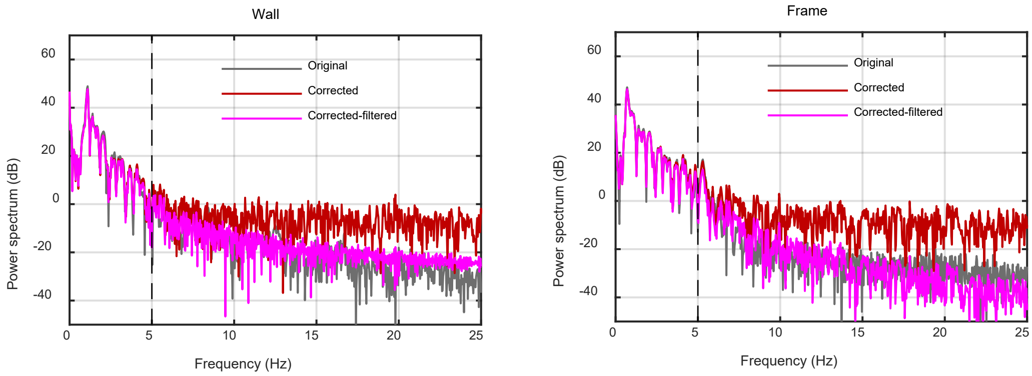

Fig. 10. Power spectrum of displacement meter measurement data

Fig. 11 presents the time history of the measured inter-story drift of the second story for seismic Case 3. Comparison between the original and corrected data reveals that floor slab rotation had a non-negligible influence on the inter-story drift measurement. In particular, the floor slab rotation exerted a greater influence on the measurement in the wall direction with an RMSE of 2.46 mm which was 2.26 times the RMSE in the frame direction. This is because the shear walls that were characterized with a flexure-type deformation mode could lead to larger floor slab rotation than the frames that were characterized with the shear-type deformation mode. Finite element analysis of the test specimen using the SAP2000 program indicated that floor slab rotation in the wall direction was approximately 2.0 times that in the frame direction at the identical lateral top displacement.

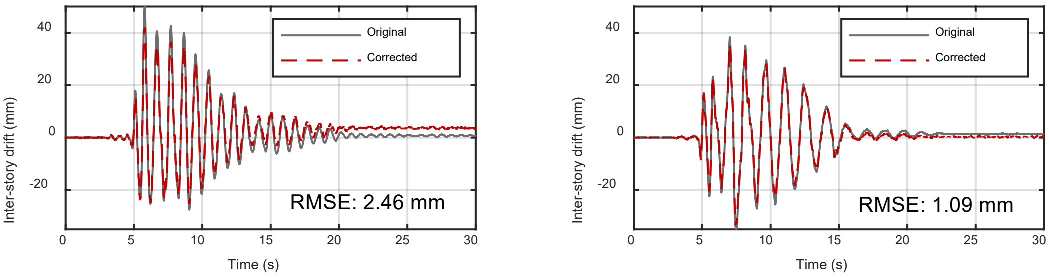

(a) Wall direction (b) Frame direction

Fig. 11. Displacement meter measurement results

The measured peak inter-story drift ratio (IDR) envelops are depicted in Fig. 12 (a) and (b). Note that the measured data was incomplete for seismic Case 6, as the maximum inter-story drifts in some stories were beyond the measurement range of the displacement meters. The discrepancy between the original and corrected data was regarded as the error induced by neglecting the floor slab rotation effect. Fig. 12 (c) and (d) shows the maximum errors of the peak inter-story drifts in different stories for a variety of loading cases. It is indicated that the drift errors induced by floor rotation generally increased with an increase of the inter-story drift levels. In addition, the drift errors in the second and third stories were obviously higher than those in the first story, which might be due to the local rotation angle of the floor would cumulatively increase along with the floor height. In the wall direction, the maximum error of inter-story drift was 14.46 mm (error/peak drift = 20.09%) and the average error was 4.54 mm. In the frame direction, the maximum and average errors were 5.36 mm (error/peak drift = 9.15%) and 1.94 mm, respectively. In the following subsections, the corrected displacement meter measurement data is used as the true measure of inter-story drifts to facilitate comparison with the results of acceleration integration measurement and computer vision-based measurement.

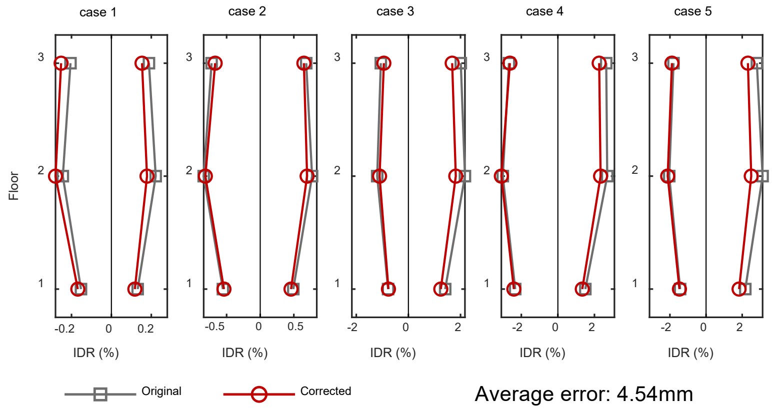

(a) Peak inter-story drift ratio in the wall direction

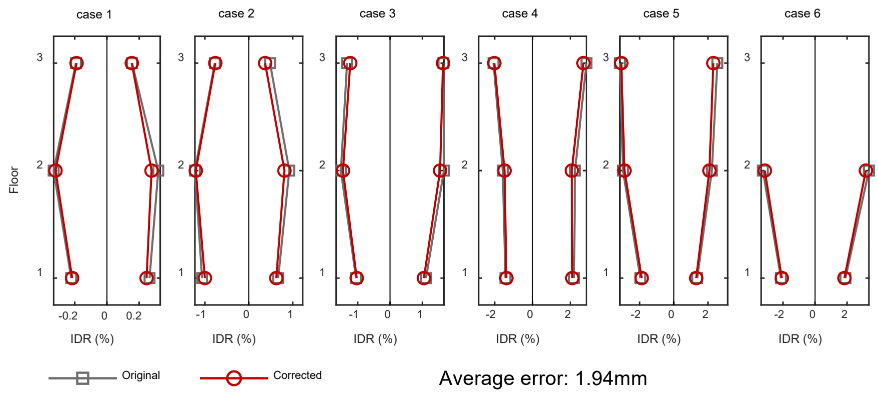

(b) Peak inter-story drift ratio in the frame direction

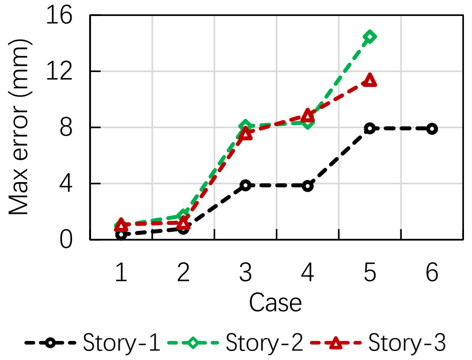

(c) Maximum error of inter-story drift in the wall direction

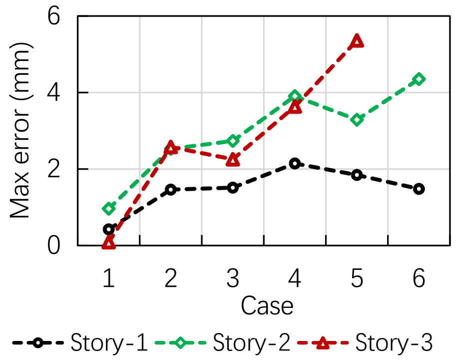

(d) Maximum error of inter-story drift in the frame direction

Fig. 12. Peak inter-story drift results measured by displacement meter

4.2 Acceleration integration measurement results

The comparison between the acceleration integration measurement results and the corrected displacement meter measurement results of seismic Case 3 is shown in Fig. 13. In this figure, the discrepancy between acceleration integration data relative to the displacement meter data is referred to as the error. Errors typically occurred when the structure underwent nonlinear responses. For this loading case, the maximum error was 4.5 mm, and was observed at the bottom story. It is noted that residual drifts were removed in the acceleration integration results due to the data being filtered by the high-pass filter. In general, the acceleration integration measurements exhibited good performance, with a SNR of 15.94 dB and RMSE of 1.41 mm for seismic Case 3.

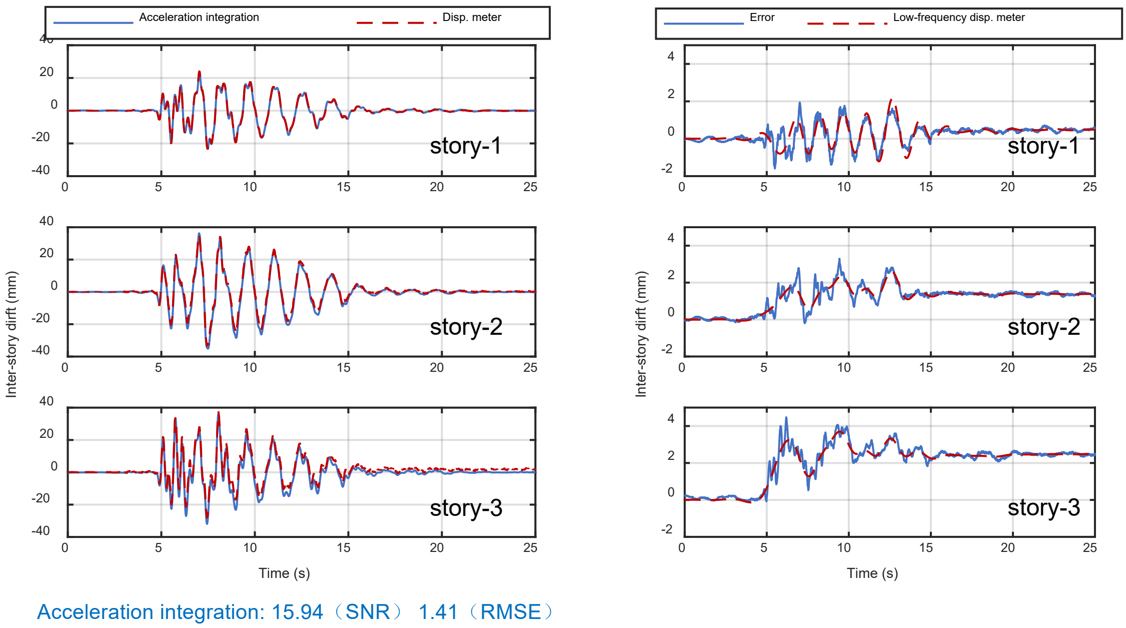

(a) Inter-story drift (b) Error

Fig. 13. Acceleration integration measurement results

The errors in the acceleration integration results are related to data processing methods. Because a high-pass filter was used in this study, the integrated results were not able to capture the structural responses at low frequencies which was removed by the filter. This was confirmed by the analysis of the data, as shown in Fig. 13(b). In this figure, the red dash line represents the low-frequency components of displacement meter measurement which were obtained using a low-pass filter with a cutoff frequency of 0.4 Hz (i.e., the cutoff frequency of the high-pass filter used in acceleration integration processing). The blue solid line represents the error of acceleration integration results. The good correlation between these two lines indicates that the error was primarily induced by filtering the low-frequency components in the acceleration integration. Comparison of power spectrum between the acceleration integration results and the displacement meter data shown in Fig.14 also confirms the above conclusions.

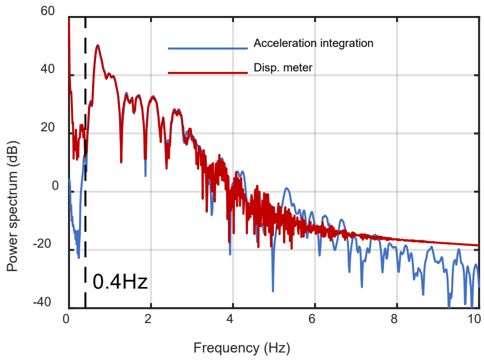

Fig. 14. Power spectrum of acceleration integration results

Fig. 15 compares the acceleration integration results and displacement meter measurements for a white noise loading case. The acceleration integration results matched displacement meter measurements well, with the SNR and RMSE values reaching 18.25 dB and 0.15 mm, respectively. This is because the response of the structure under the white noise excitation was small (less than 0.2% drift) and the structure remained in elastic without nonlinear response and residual drifts.

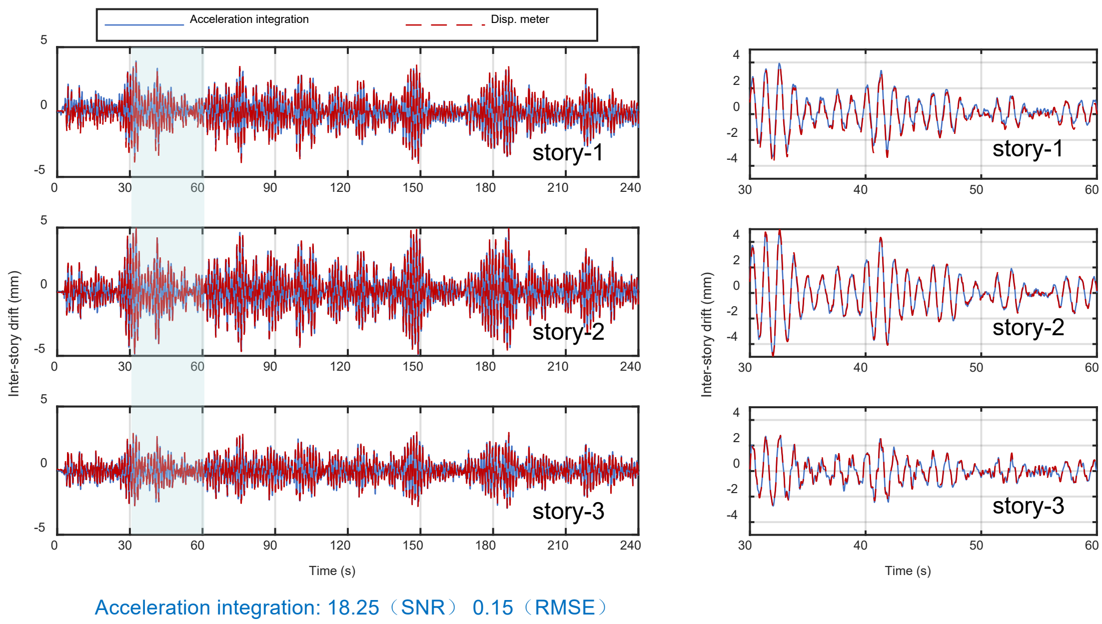

(a) Inter-story drift (b) Zoomed-in view

Fig. 15. Acceleration integration measurement results under white noise excitation

4.3 Computer vision-based measurement results

Fig. 16 illustrates the computer vision-based measurement results of seismic Case 3, in which both the traditional template matching method and the proposed SR target tracking method were compared. While both vision-based measurements appeared to correlate with the displacement meter measurement results, a zoomed-in view indicates that the conventional template matching measurement curve was saw-toothed. This is because the scale factor of the image is 4.5 mm/pixel which led to a minimum resolution for the conventional method of 4.5 mm. However, the proposed SR method can track the sub-pixel target displacement, and thus exhibited improved measurement accuracy. Compared to conventional template matching tracking, the SR target tracking increased the SNR by 68% and decreased the RMSE by 63%.

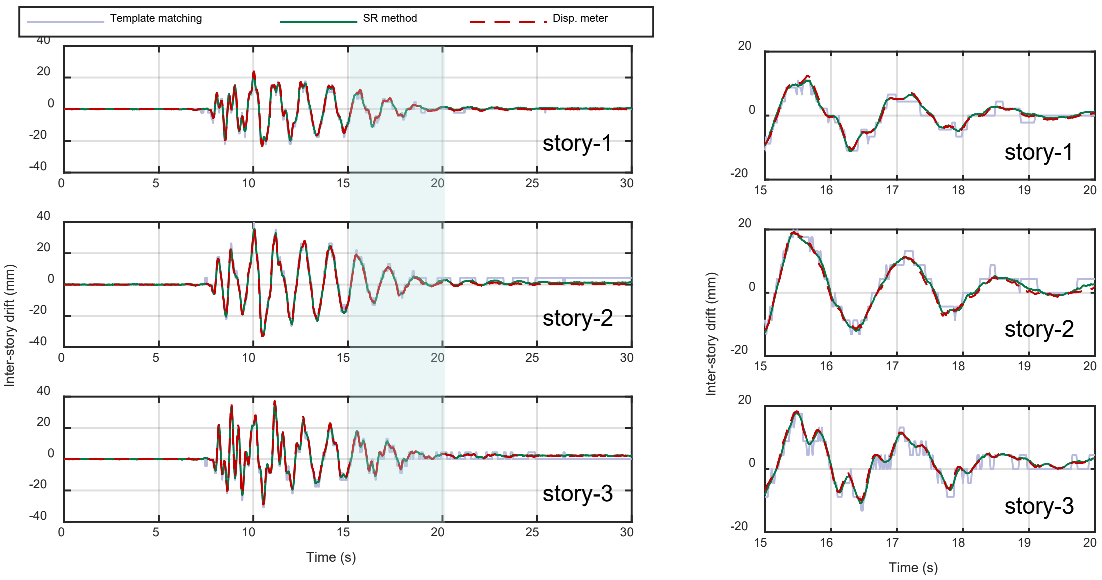

Template matching: 12.46（SNR） 1.88（RMSE）
SR method：21.00（SNR） 0.69（RMSE）

(a) Inter-story drift (b) Zoomed-in view

Fig. 16. Computer vision-based measurement results

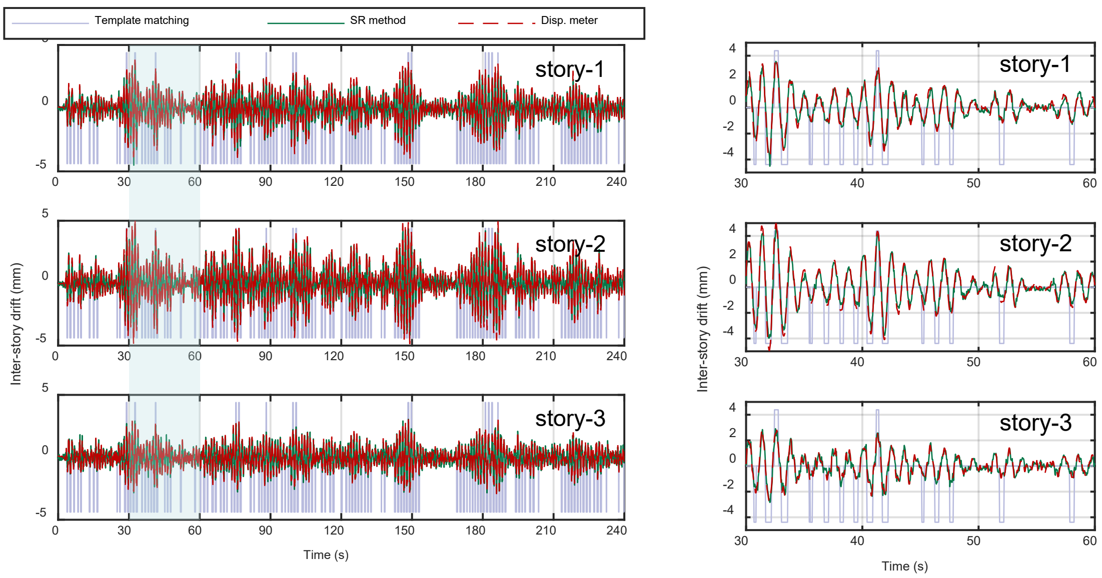

Template matching: -3.81（SNR） 1.81（RMSE）
SR method：12.74（SNR） 0.29（RMSE）

(a) Inter-story drift (b) Zoomed-in view

Fig. 17. Computer vision-based measurement results under white noise excitation

The white noise vibration data, as depicted in Fig. 17, clearly demonstrates the improvement of the SR method relative to the traditional template matching measurement. Because most drift responses were smaller than 4.5 mm, which equals to the minimum resolution, the traditional template matching measurement method could not accurately measure the drift history. Due to the capability of sub-pixel target tracking, the developed SR method can accurately measure such small displacement responses. The SNR of the SR measurement results reached 12.74 dB, and the RMSE was 0.29 mm for the white noise case.

The aforementioned vision-based analysis was run on a computer with Intel i7-6850 CPU, NVIDIA RTX 3090Ti GPU and 32 Gb RAM. The processing of conventional template matching was simple and it cost 0.19 s for one picture. The SR target tracking were divided into three steps: conventional template matching, the SR reconstruction of ROIs and multi-region tracking, which took 0.19, 0.21, and 0.71s respectively for analysis of one picture. GPU acceleration was implemented only in the step of SR reconstruction of ROIs.

4.4 Comparison of different measurement methods

Fig. 18 presents the SNR of the measurement results using the acceleration integration method and vision-based SR method for the six seismic loading cases and four white noise excitation cases. For the seismic loading cases, the SNR of acceleration integration results generally decreased along with an increase in the structural nonlinear responses, as an increased nonlinear response would lead to a rise in low-frequency responses and residual drifts. From JMA Kobe-0.07g shaking to Takatori-0.62g shaking, the SNR value of drifts measured by the acceleration integration decreased from 18.46 dB to 8.36 dB. It is noted that the procedure of acceleration integration (as detailed in subsection 3.3) needs the calibration with displacement meter measurement to determine the cutoff frequency. Without such information, the cutoff frequency would be most probably set by engineer judgement which may lead to an increased error. However, the vision-based SR method showed increasing SNR values along with an increase in structural responses ranging from 18.26 dB to 26.26

dB. This is because the measurement error was almost identical for all cases as the image resolution was identical. Therefore, the increase in responses resulted in the increase in SNR. For the white noise cases, the acceleration integration method maintained a stable and good accuracy with an average SNR of 17.85 dB, and the vision-based SR method had an average SNR of 12.48 dB.

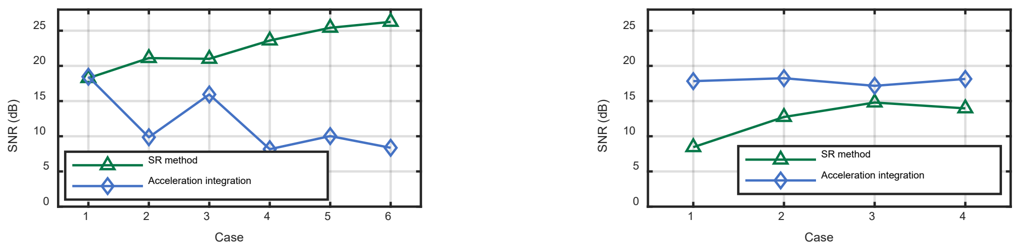

(a) SNR of seismic cases   (b) SNR of white noise cases

Fig. 18. Signal quality comparison of different measurement methods

Fig. 19(a) depicts the peak inter-story drifts measured by different methods for the seismic loading cases. Fig. 19(b) indicates that the error of the acceleration integration results increased according to the structural displacement responses. The acceleration integration measurement results had an average error of 2.61 mm and a maximum error of 10.16 mm. As indicated in Fig. 19(c), the SR method provided highly accurate drift measurements with an average and maximum error of 0.80 mm and 3.73 mm, respectively.

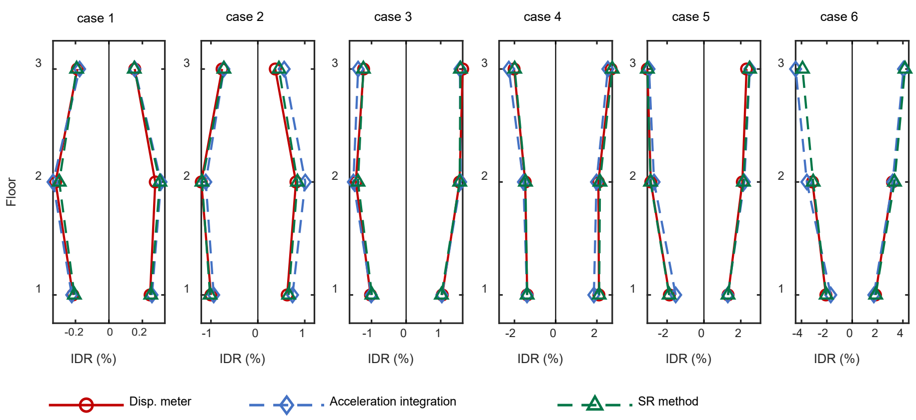

(a) Inter-story drift ratio

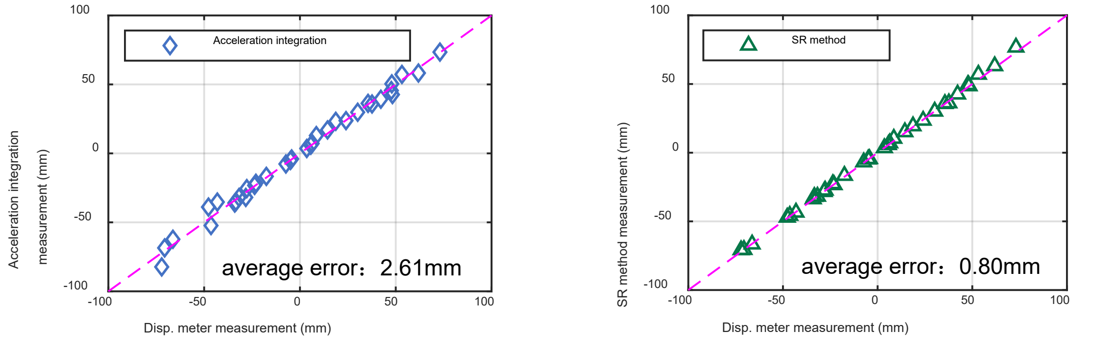

(b) Inter-story drift from acceleration integration method

(c) Inter-story drift from SR method

Fig. 19. Inter-story drift results of different methods

Residual drifts are an essential measure for evaluating the recoverability of a structure after an earthquake [47]. As illustrated in Fig. 20, the vision-based SR method exhibited excellent performance in measuring the residual drifts of the structure after seismic shaking. However, the acceleration integration method cannot capture the residual drifts of the structure due to use of high-pass filter in data processing.

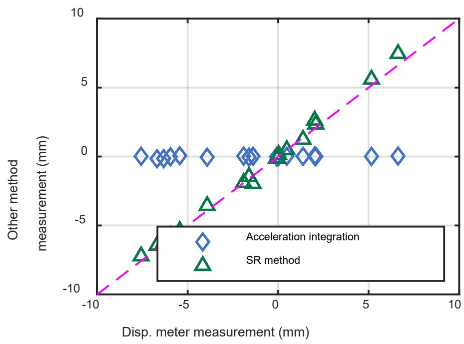

Fig. 20. Residual drift measurement results

5 DISCUSSIONS

5.1 Noise amplification of displacement meter measurement

The displacement meter data correction method could eliminate the floor slab rotation influence while the correction process may amplify the measurement noise (Fig. 10). Assuming that the measurement noise of each displacement meter is independent and identically distributed, the measurement result of each displacement meter can be defined as follows:

$$d = A + N_d \tag{14}$$

where d is the measurement data of the displacement meter, A is the actual displacement, and N_d is the measurement noise, which follows a distribution with an expected value of zero and the variance of σ^2. The variance of D_{i1}, D_{i2}, D_{i3}, D_f was calculated based on Eqs. (1) – (6). The results are shown in Eqs. (15) - (18), which quantified the effects of noise amplification. For the second story inter-story drift response, the variance of corrected inter-story drift D_{if} was 80.6 times the variance of the original inter-story drift D_{i2}. In the low-frequency region, the structural response was significantly higher than the measurement noise, and thus, the noise amplification effect was not obvious. However, in the high-frequency region, noises significantly contributed to the measurement data, and hence the noise amplification effect was noticeable, as indicated in Fig. 10. Calculations using Eq. (18) indicates that the amplified noise had an increase of the power spectrum by 19.1 dB, which is consistent with the observations in Fig. 10. To control the influence of noise amplification, it is recommended to select h_i greater than $0.1H$.

$$\sigma^2(D_{i1}) = \begin{cases} 0 & , \quad i = 1 \\ \sum_{k=1}^{i-1} 2(H_i/h_k)^2\sigma^2, & i > 1 \end{cases} \tag{15}$$

$$\sigma^2(D_{i2}) = \sigma^2/2 \tag{16}$$

$$\sigma^2(D_{i3}) = 2(L_i/h_i)^2\sigma^2 \tag{17}$$

$$\sigma^2(D_{if}) = \sigma^2(D_{i1}) + (L_i/h_i + 0.5)^2\sigma^2 + (L_i/h_i - 0.5)^2\sigma^2 \tag{18}$$

5.2 Multi-region tracking

Target selection is crucial for the cross-correlation template matching approach, which calculates the cross-correlation between the target and the image to determine the target position. In the process of template matching, one entire stiff region on the structure surface is commonly chosen as the target. This is performed not only for convenience but also to match a greater number of pixels for more stable results. Nevertheless, the minimum resolution for tracking a single region is generally one pixel which indicates that the tracking error is at the pixel level. To minimize the error, more regions can be matched to achieve smaller resolution and error variance, assuming that the tracking error is independent of the size of the matched target.

To explore whether multi-region matching can improve the matching accuracy, single-region tracking and multi-region tracking were employed to obtain the position of targets in the SR images, and the quality of the obtained inter-story drift was compared, as shown in Fig. 21. The multi-region tracking performed better in tracking white noise vibrations, with an average SNR gain of 15.0% (1.67 dB) and a reduction in RMSE of 13.9% (0.043 mm), while there was no remarkable difference between the two tracking approaches for seismic vibrations.

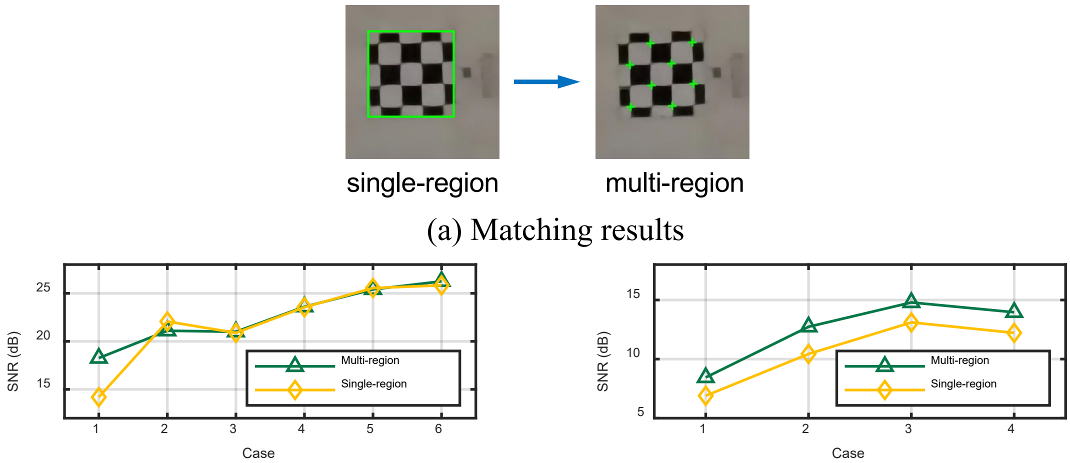

(a) Matching results

(b) SNR of seismic Cases

(c) SNR of white noise Cases

Fig. 21. Comparison of single-region and multi-region tracking

5.3 Identification of structural modal parameters

While system identification is commonly based on acceleration data, accurately measured dynamic displacement responses from the vision-based method may also serve as useful data. Because the traditional vision-based measurement is often constrained by the low resolution of the global-view video of a large-scale shaking table test specimen, it cannot provide accurate displacement data for system identification. The novel SR target tracking method may overcome this resolution restraint and achieve precise measurements of small-magnitude responses of white noise vibrations.

The autoregressive (AR) with exogenous term (ARX) method [48] was adopted for system identification from the vision-based SR measurement data of displacement responses for the white noise excitation Case 2. The displacement of the bottom floor was taken as the input, and the displacement responses at the first to third floors as the output. Fig. 22 displays the identified dynamic properties, including the first three natural vibration frequencies, damping ratios and corresponding mode shapes in the frame direction. The dynamic properties identified from the acceleration data in this white noise excitation case were also included for comparison. As indicated in the figure, the identified frequencies and mode shapes from two sets of data correlated well, with a frequency difference of less than 2% and a modal assurance criterion (MAC) of mode shapes greater than 0.98. The damping ratios of the first two modes were also accurately identified from the SR measurement data, while that of the third mode was larger than the value identified from the acceleration data. This is because the high-mode effect made significantly less contribution to the displacement responses than the acceleration responses. Therefore, the SNR of SR measured displacement at the frequency band of the third mode was lower than that of the acceleration recorded by accelerometers, which resulted in less accuracy in the damping identification of the third mode from the SR measurement data. Nevertheless, the SR measurement data generated satisfactory results for system identification.

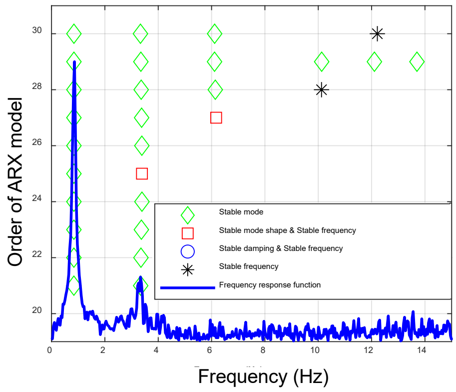

(a) Stabilization diagram

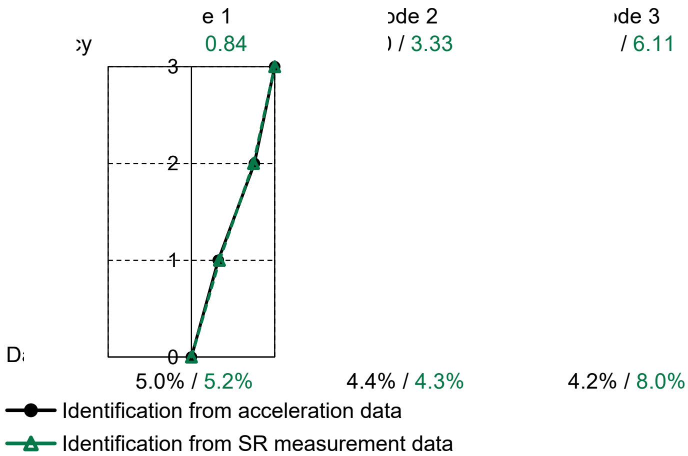

(b) Dynamic properties

Fig. 22. Identification of structural modal parameters

6 CONCLUSIONS

This study compared three commonly-used approaches of inter-story drift measurement of shaking table tests, and developed the associated techniques for enhanced measurement. A novel arrangement of displacement meters and an associated data correction method were proposed to eliminate the influence of floor slab rotations on inter-story drift measurement, and a novel object tracking method based on super-resolution (SR) image reconstruction was developed to realize stable sub-pixel displacement measurement. Shaking table tests of a large-scale three-story RC building structure were used as a case study to evaluate the accuracy of these measurement approaches. The major conclusions derived from this study are as follows:

(1) The floor slab rotation affected the accuracy of the measured inter-story drift data of displacement meters set at the overhanging steel arms between adjacent floors. This resulted in errors of approximately 20% in measuring inter-story drift for the shaking table tests in this study. By setting the overhanging steel arms above and beneath a floor slab in the same position, this proposed arrangement of displacement meters and associated data correction method effectively eliminated the influence of floor slab rotation.

(2) For the acceleration integration method, use of high-pass filtering can remove baseline drift while resulting in the loss of residual displacement and errors of inter-story drifts in the low-frequency region. The test data indicates that the acceleration integration method generated increased errors in line with the increase in structural nonlinear responses, which reached 10.16 mm (error/peak = 14%) for the shaking table tests in this study.

(3) The developed SR target tracking method combines the deep learning-based SR technique with the traditional cross-correlation template matching algorithm. The application of the SR method in the RC structure shaking table tests indicated that this method overcame the limitation of video resolution and achieved a stable sub-pixel displacement measurement. In a seismic loading case, the SR method improved the SNR of the drift measurement by 68% and reduced RMSE by 63%, compared with the traditional template matching method.

(4) The SR target tracking method provided precise measurements of small-magnitude displacement responses of the test structure under white noise excitations. From these displacement data, the structural modal parameters were extracted using system identification. The identified modal parameters closely matched those extracted from acceleration data, with a frequency error less than 2% and a MAC of mode shapes greater than 0.98.

ACKNOWLEDGEMENT

This study was supported by the National Natural Science Foundation of China (Grant No. 52078277) and the National Key R&D Program of China (Grant No. 2017YFC1500602). The authors wish to express their sincere gratitude to the sponsors. The authors also thank Dr. Wenjie Liao at Tsinghua University for his discussions and suggestions on this study.

REFERENCES

[1] Nakashima M, Nagae T, Enokida R, et al. Experiences, accomplishments, lessons, and challenges of E-defense—Tests using world's largest shaking table[J]. *Japan Architectural Review*, 2018, 1(1): 4-17. https://doi.org/10.1002/2475-8876.10020

[2] Sun Z, Chen Y, Xu S Y, et al. Shaking table test of concrete columns hybrid reinforced by steel/FRP bars[J]. *Journal of Building Engineering*, 2022, 48: 103938. https://doi.org/10.1016/j.jobe.2021.103938

[3] Van de Lindt J W, Pei S, Pryor S E, et al. Experimental seismic response of a full-scale six-story light-frame wood building[J]. *Journal of Structural Engineering*, 2010, 136(10): 1262-1272. https://doi.org/10.1061/(ASCE)ST.1943-541X.0000222

[4] Wang X, Hutchinson T C, Astroza R, et al. Shake table testing of an elevator system in a full-scale five-story building [J]. *Earthquake Engineering & Structural Dynamics*, 2017, 46: 391-407. https://doi.org/10.1002/eqe.2793

[5] Ji X, Kajiwara K, Nagae T, et al. A substructure shaking table test for reproduction of earthquake responses of high-rise buildings[J]. *Earthquake Engineering & Structural Dynamics*, 2009, 38(12): 1381-1399. https://doi.org/10.1002/eqe.907

[6] Yu E, Skolnik D, Whang D H, et al. Forced vibration testing of a four-story reinforced concrete building utilizing the nees@ UCLA mobile field laboratory[J]. *Earthquake Spectra*, 2008, 24(4): 969-995. https://doi.org/10.1193/1.2991300

[7] Kajiwara K, Tosauchi Y, Kang J D, et al. Shaking-table tests of a full-scale ten-story reinforced-concrete building (FY2015). Phase I: free-standing system with base sliding and uplifting[J]. *Engineering Structures*, 2021, 233: 111848. https://doi.org/10.1016/j.engstruct.2020.111848

[8] Zhang A, Xie Z, Zhang Y, et al. Shaking table test of a prefabricated steel frame structure with all-bolted connections[J]. *Engineering Structures*, 2021, 248: 113273. https://doi.org/10.1016/j.engstruct.2021.113273

[9] Filiatrault A, Christovasilis I P, Wanitkorkul A, et al. Experimental seismic response of a full-scale light-frame wood building[J]. *Journal of Structural Engineering*, 2010, 136(3): 246-254. https://doi.org/10.1061/(ASCE)ST.1943-541X.0000112

[10] Yenidogan C, Nishi R, Uwadan S, et al. Full-scale shake table tests of P&B type of Japanese three-story wood dwellings for the collapse characterization[J]. *Soil Dynamics and Earthquake Engineering*, 2021, 150: 106898. https://doi.org/10.1016/j.soildyn.2021.106898

[11] Tian S, Gardoni P, Li H, et al. Baseline correction of ground motions with physics-based correction patterns[J]. *Geophysical Journal International*, 2019, 217(1): 668-681. https://doi.org/10.1093/gji/ggz039

[12] Skolnik D A, Wallace J W. Critical assessment of interstory drift measurements[J]. *Journal of Structural Engineering*, 2010, 136(12): 1574-1584. https://doi.org/10.1061/(ASCE)ST.1943-541X.0000255

[13] Dai Z, Li X, Chen S, et al. Baseline correction based on L1-Norm optimization and its verification by a computer vision method[J]. *Soil Dynamics and Earthquake Engineering*, 2020, 131: 106047. https://doi.org/10.1016/j.soildyn.2020.106047

[14] Clemente P, Bongiovanni G, Buffarini G, et al. Effectiveness of HDRB isolation systems under low energy earthquakes[J]. *Soil Dynamics and Earthquake Engineering*, 2019, 118: 207-220. https://doi.org/10.1016/j.soildyn.2018.12.018

[15] Saranik M, Lenoir D, Jézéquel L. Shaking table test and numerical damage behaviour analysis of a steel portal frame with bolted connections[J]. *Computers & structures*, 2012, 112: 327-341. https://doi.org/10.1016/j.compstruc.2012.07.009

[16] Wang R, Schurr B, Milkereit C, et al. An improved automatic scheme for empirical baseline correction of digital strong-motion records[J]. *Bulletin of the Seismological Society of America*, 2011, 101(5): 2029-2044. https://doi.org/10.1785/0120110039

[17] Chiou B, Darragh R, Gregor N, et al. NGA project strong-motion database[J]. *Earthquake Spectra*, 2008, 24(1): 23-44. https://doi.org/10.1193/1.2894831

[18] Akkar S, Sandıkkaya M A, Şenyurt M, et al. Reference database for seismic ground-motion in Europe (RESORCE)[J]. *Bulletin of Earthquake Engineering*, 2014, 12(1): 311-339. https://doi.org/10.1007/s10518-013-9506-8

[19] Ji X, Miao Z, Kromanis R. Vision-based measurements of deformations and cracks for RC structure tests[J]. *Engineering Structures*, 2020, 212: 110508. https://doi.org/10.1016/j.engstruct.2020.110508

[20] Chen C C, Wu W H, Tseng H Z, et al. Application of digital photogrammetry techniques in identifying the mode shape ratios of stay cables with multiple camcorders[J]. *Measurement*, 2015, 75: 134-146. https://doi.org/10.1016/j.measurement.2015.07.037

[21] Ye X W, Dong C Z, Liu T. Image-based structural dynamic displacement measurement using different

multi-object tracking algorithms[J]. *Smart Structures and Systems*, 2016, 17(6): 935-956. https://doi.org/10.12989/sss.2016.17.6.935

[22] Khaloo A, Lattanzi D. Pixel-wise structural motion tracking from rectified repurposed videos[J]. *Structural Control and Health Monitoring*, 2017, 24(11): e2009. https://doi.org/10.1002/stc.2009

[23] Jiao J, Guo J, Fujita K. Displacement measurement and nonlinear structural system identification: A vision-based approach with camera motion correction using planar structures. *Structural Control and Health Monitoring*, 2021, 28(8): e2761. https://doi.org/10.1002/stc.2761

[24] Khuc T, Catbas F N. Computer vision-based displacement and vibration monitoring without using physical target on structures[J]. *Structure and Infrastructure Engineering*, 2017, 13(4): 505-516. https://doi.org/10.1080/15732479.2016.1164729

[25] Jeong J H, Jo H. Real-time generic target tracking for structural displacement monitoring under environmental uncertainties via deep learning[J]. *Structural Control and Health Monitoring*, 2022, 29(3): e2902. https://doi.org/10.1002/stc.2902

[26] Xiang C, Wang W, Deng L, et al. Crack detection algorithm for concrete structures based on super-resolution reconstruction and segmentation network[J]. *Automation in Construction*, 2022, 140: 104346. https://doi.org/10.1016/j.autcon.2022.104346

[27] Yang T, Jia S, Ma H. Research on the application of super resolution reconstruction algorithm for underwater image[J]. *Computers, Materials & Continua*, 2020, 62(3): 1249-1258. https://doi.org/10.32604/cmc.2020.05777

[28] Sun C, Gu D, Zhang Y, et al. Vision-based displacement measurement enhanced by super-resolution using generative adversarial networks[J]. *Structural Control and Health Monitoring*, 2022: e3048. https://doi.org/10.1002/stc.3048

[29] Courtrai L, Pham M T, Lefèvre S. Small object detection in remote sensing images based on super-resolution with auxiliary generative adversarial networks[J]. *Remote Sensing*, 2020, 12(19): 3152. https://doi.org/10.3390/rs12193152

[30] Lei S, Shi Z, Zou Z. Super-resolution for remote sensing images via local-global combined network[J]. *IEEE Geoscience and Remote Sensing Letters*, 2017, 14(8): 1243-1247. DOI: 10.1109/LGRS.2017.2704122

[31] Liu H, Liu J, Hou S, et al. Perception consistency ultrasound image super-resolution via self-supervised CycleGAN[J]. *Neural Computing and Applications*, 2021: 1-11. https://doi.org/10.1007/s00521-020-05687-9

[32] Fang L, Monroe F, Novak S W, et al. Deep learning-based point-scanning super-resolution imaging[J]. *Nature methods*, 2021, 18(4): 406-416. DOI: 10.1038/s41592-021-01080-z

[33] Luo L, Feng M Q, Wu Z Y. Robust vision sensor for multi-point displacement monitoring of bridges in the field[J]. *Engineering Structures*, 2018, 163: 255-266. https://doi.org/10.1016/j.engstruct.2018.02.014

[34] Feng D, Feng M Q. Vision-based multipoint displacement measurement for structural health monitoring[J]. *Structural Control and Health Monitoring*, 2016, 23(5): 876-890. https://doi.org/10.1002/stc.1819

[35] Wu Z Y, Shenton III H W, Mo D, et al. Integrated video analysis framework for vision-based comparison study on structural displacement and tilt measurements[J]. *Journal of Structural Engineering*, 2021, 147(9): 05021005. https://doi.org/10.1061/(ASCE)ST.1943-541X.0003104
[36] Keys R. Cubic convolution interpolation for digital image processing[J]. *IEEE Transactions on Acoustics, Speech, and Signal Processing*, 1981, 29(6): 1153-1160. DOI:10.1109/TASSP.1981.1163711
[37] Parker J A, Kenyon R V, Troxel D E. Comparison of interpolating methods for image resampling[J]. *IEEE Transactions on Medical Imaging*, 1983, 2(1): 31-39. DOI: 10.1109/TMI.1983.4307610
[38] Jiang M, Wang G. Development of iterative algorithms for image reconstruction[J]. *Journal of X-ray Science and Technology*, 2002, 10(1-2): 77-86.
[39] Wang Z, Liu D, Yang J, et al. Deep networks for image super-resolution with sparse prior[C]. *Proceedings of the IEEE International Conference on Computer Vision (ICCV)*. 2015: 370-378.
[40] Dong C, Loy C C, He K, et al. Learning a deep convolutional network for image super-resolution[C]. *European Conference on Computer Vision (ECCV)*. Springer, Cham, 2014: 184-199.
[41] Yang W, Zhang X, Tian Y, et al. Deep learning for single image super-resolution: A brief review[J]. *IEEE Transactions on Multimedia*, 2019, 21(12): 3106-3121. DOI: 10.1109/TMM.2019.2919431
[42] Li Z, Yang J, Liu Z, et al. Feedback network for image super-resolution[C]. *Proceedings of the IEEE/CVF Conference on Computer Vision and Pattern Recognition (CVPR)*. 2019: 3867-3876.
[43] Wang Z, Bovik A C, Sheikh H R, et al. Image quality assessment: from error visibility to structural similarity[J]. *IEEE Transactions on Image Processing*, 2004, 13(4): 600-612. DOI: 10.1109/TIP.2003.819861
[44] Ji X, Zhuang Y, Miao Z. et al. Vision-based seismic damage detection and residual capacity assessment for an RC shaking table test structure[J]. *Earthquake Engineering & Structural Dynamics*, 2022. DOI: 10.1002/eqe.3788
[45] Zhang Y Q, Song J J, Tu L Y, et al. Error analysis and improvement method when numerical integration with software[J]. *Journal of Mechanical Strength*, 2006(03):419-423. DOI:10.16579/j.issn.1001.9669.2006.03.023. (in Chinese)
[46] Ye X W, Dong C Z. Review of computer vision-based structural displacement monitoring[J]. *China Journal of Highway and Transport*, 2019, 32(11): 21. (in Chinese)
[47] Ruiz-García J, Miranda E. Residual displacement ratios for assessment of existing structures[J]. *Earthquake Engineering & Structural Dynamics*, 2006, 35(3): 315-336. https://doi.org/10.1002/eqe.523
[48] Ji X, Fenves G L, Kajiwara K, et al. Seismic damage detection of a full-scale shaking table test structure[J]. *Journal of Structural Engineering*, 2011, 137(1): 14-21. https://doi.org/10.1061/(ASCE)ST.1943-541X.0000278